Supporting Information for

High efficiency ion exchange doping of conducting polymers

Ian E. Jacobs, Yue Lin, Yuxuan Huang, Xinglong Ren, Dimitrios Simatos, Chen Chen, Dion Tjhe, Martin Statz, Lianglun Lai, Peter A. Finn, William G. Neal, Gabriele D'Avino, Vincent Lemaur, Simone Fratini, David Beljonne, Joseph Strzalka, Christian B. Nielsen, Stephen Barlow, Seth R. Marder, Iain McCulloch, Henning Sirringhaus

June 18, 2021

This PDF file includes:
Figures S1-S16, Tables S1-S5, and supporting discussion

1 Theory of ion exchange doping

1.1 Charge transfer equilibrium

We can derive the charge transfer equilibrium for a generic dopant from the charge transfer reaction,

$$\mathrm{P}_f + \mathrm{D}_s{}^0 \overset{\mathrm{k_{ct}}}{\rightleftharpoons} [\mathrm{P}_f{}^+ \mathrm{D}_f{}^-] \tag{1}$$

where P is the polymer and D is a p-type dopant, subscripts indicate the phase (film or solution), and superscripts indicate the charge. The product of this reaction is assumed to be a tightly bound integer charge transfer complex (integer CTC); therefore the reverse reaction is first order while the forward reaction is second order,

$$r_1 = k_1 C^0_{D,s} N^0 \tag{2}$$

$$r_{-1} = k_{-1} C^-_{D,f} \tag{3}$$

where $C^z_{i,x}$ is the concentration of species i, in phase x, with charge z, and N^0 is the density of neutral sites in the polymer. At equilibrium, the forward and reverse rates are equal. Therefore, we can define the equilibrium constant as

$$k_{ct} = \frac{k_1}{k_{-1}} = \frac{C^-_{D,f}}{C^0_{D,s} N^0} \tag{4}$$

Assuming only singly ionized sites occur, the total density of sites in the polymer is the sum of the neutral and ionized sites,

$$N_{tot} = N^0 + N^+ \tag{5}$$

Solving Equation 4 for N^0, substituting into Equation 5, and rearranging, we obtain

$$\frac{C^-_{D,f}}{N_{tot}} = \frac{N^+}{N_{tot}} = \Theta = \frac{k_{ct} C^0_{D,s}}{1 + k_{ct} C^0_{D,s}} \tag{6}$$

This is the Langmuir isotherm, which describes the fraction of sites in the polymer which are doped for a given equilibrium constant and concentration of neutral dopant in solution. Previous work has demonstrated that this model accurately describes ionization in P3HT:F4TCNQ at relatively low doping levels.[1–3] This model implicitly assumes each site within the polymer is non-interacting, however the Arkhipov model[4] discussed in the main text suggests that as the Coulomb wells of the dopant overlap, ionization should become progressively more difficult. Nonetheless, this model is still instructive in demonstrating how ion exchange couples to the charge transfer reaction.

1.2 Ion exchange equilibrium

We derive the ion exchange equilibrium following the same steps used above. The ion exchange reaction is written as:

$$\mathrm{D}_f{}^- + \mathrm{A}_s{}^- \underset{}{\overset{\mathrm{k_{ex}}}{\rightleftharpoons}} \mathrm{D}_s{}^- + \mathrm{A}_f{}^- \tag{7}$$

The rate equations are

$$r_2 = k_2 C^-_{D,f} C^-_{A,s} \tag{8}$$

$$r_{-2} = k_{-2} C^-_{D,s} C^-_{A,f} \tag{9}$$

Setting the the forward and reverse rates equal to each other yields the selectivity coefficient.

$$k_{ex} = \frac{k_2}{k_{-2}} = \frac{C^-_{A,f} C^-_{D,s}}{C^-_{A,s} C^-_{D,f}} \tag{10}$$

It's important to note that although the selectivity coefficient is unitless, its value depends on the units used to express the concentrations. Here, we will use molar concentrations, therefore in this work k_{ex} is the the molar selectivity coefficient. Furthermore, although the selectivity coefficient is a type of equilibrium coefficient, strictly speaking it is distinct from the true thermodynamic equilibrium coefficient, which is defined in terms of activities rather than concentrations. A detailed discussion including generalization to higher valence ions is given by Helfferich.[5]

To derive the ion exchange isotherm, we define the mole fraction of each ion in the film $x_i = \frac{C^-_{i,f}}{N^+}$ where N^+ is the density of ionized sites in the polymer, $N^+ = C^-_{A,f} + C^-_{D,f}$. Substituting this expression into Equation 10, using $x_A + x_D = 1$ and rearranging gives the ion exchange isotherm,

$$\frac{C^-_{A,f}}{N^+} = x_A = \frac{k_{ex} C^-_{A,s}}{C^-_{D,s} + k_{ex} C^-_{A,s}} \tag{11}$$

This equation describes what proportion of ionized sites in the polymer contain an electrolyte anion A^-. The mole fraction of sites which still contain the dopant ion, D^-, which is what we measure experimentally, is $x_D = 1 - x_A$. In Equation 11 the concentration of dopant ions in solution, $C^-_{D,s}$, is not directly known. However, since $FeCl_3$ disproportionates upon dissolution, the concentration of $FeCl_4^-$ in solution is only slightly less than the original $FeCl_3$ concentration (see Figure S2). $C^-_{D,s}$ can be approximated as 3/4 the original $FeCl_3$ concentration, as discussed in Section 2.2.1.

1.3 Coupled ion exchange and charge transfer equilibria

The overall ion exchange doping reaction is the product of the charge transfer reaction (Equation 1) and the ion exchange reaction (Equation 7),

$$\mathrm{P}_f + \mathrm{D}_s{}^0 + \mathrm{A}_s{}^- \underset{}{\overset{\mathrm{k_{tot}}}{\rightleftharpoons}} [\mathrm{P}_f{}^+ \mathrm{A}_f{}^-] + D^-_s \tag{12}$$

Note that this reaction implicitly assumes negligible doping by $FeCl_4^-$, i.e. the exchange efficiency is assumed to be 100%. For sequential reactions, the equilibrium coefficient is the product of the equilibrium coefficient for each reaction,

$$k_{tot} = k_{ct}k_{ex} = \frac{C_{D,f}^-}{C_{D,s}^0 N^0}\frac{C_{A,f}^- C_{D,s}^-}{C_{A,s}^- C_{D,f}^-} = \frac{C_{D,s}^-}{C_{D,s}^0}\frac{C_{A,f}^-}{N^0 C_{A,s}^-} \tag{13}$$

By grouping terms involving the dopant and the electrolyte anion, it becomes apparent that when exchange efficiency is high and *at equilibrium*, the overall reaction can be described as purely interfacial electron transfer reaction between the polymer and dopant which occurs concurrently with ion injection into the film. When the system is not at equilibrium, there may still be significant injection of D^- into the film, if for example these ions diffuse into the film much more quickly than the A^- ions.

Following this thread, we can more clearly understand the coupled charge transfer and ion exchange equilibria by rewriting the reactions given in Equations 1 and 7 as a set of elementary reactions,

$$P_f \overset{k_{ox,P}}{\rightleftharpoons} {P_f}^+ + e^- \tag{14}$$

$$e^- + {D_s}^0 \overset{k_{red,D}}{\rightleftharpoons} {D_s}^- \tag{15}$$

$${A_s}^- \overset{k_{inj,A}}{\rightleftharpoons} {A_f}^- \tag{16}$$

$$[{P_f}^+ {A_f}^-] \overset{k_{eh,A}}{\rightleftharpoons} {P_f}^+ + {A_f}^- \tag{17}$$

$${D_s}^- \overset{k_{inj,D}}{\rightleftharpoons} {D_f}^- \tag{18}$$

$$[{P_f}^+ {D_f}^-] \overset{k_{eh,D}}{\rightleftharpoons} {P_f}^+ + {D_f}^- \tag{19}$$

In this framework, the overall doping reaction corresponds to a sum of Equation 14 + 15 + 16 - 17, with equilibrium constant $\frac{k_{ox,P}k_{red,D}k_{inj,A}}{k_{eh,A}}$.

For comparison, the reaction for electrochemical doping of polymer P with electrolyte anion A corresponds to polymer oxidation, ion insertion, and formation of a polaron-ion CTC; that is, Equations 14 + 16 - 17. Thus, we can see the only difference between an electrochemical doping process and ion exchange doping is Equation 15, which is simply the solution-state dopant redox reaction as measured by e.g. cyclic voltammetry. In this sense, it becomes clear that when ion exchange is efficient, ion exchange doping is identical to electrochemical doping with an applied voltage equal to the reduction potential of species D, corresponding to the E^0 of Equation 17, which can be directly measured by cyclic voltammetry.

Therefore, for a fixed electrolyte concentration, and under conditions when ion exchange is efficient, (i.e. there is negligible injection of the dopant ion into the film), the doping reaction equilibrium should be directly proportional to the dopant reduction potential measured by CV in the same electrolyte. Under these conditions the dopant should more properly be called an oxidizing agent. More importantly, though, it suggests that a combination of ion exchange doping and electrochemical experiments can be used to directly measure the energetic shifts calculated by Li *et al.*[6]

2 Dopant characterization

2.1 Cyclic Voltammetry

The formalism given in Section 1.3 and Figure 3 of the main paper suggests a direct correspondence between electrochemical device measurements and redox potentials measured in the same electrolyte. To support this theory, we measured the redox potential, E_D^0 of each dopant in conditions identical to those used for ion exchange, i.e. 100 mM BMP TFSI in dry acetonitrile under nitrogen.

Our CV measurements were performed using a PalmSens4 potentiostat using platinum working and counter electrodes. We used an oxidized silver quasi-reference electrode prepared by exposing a clean silver

wire to oxygen plasma (300 W) for one minute. This reference was chosen over the more common AgCl quasi-reference to match the electrode used in our OECT devices, where halide impurities could potentially affect device performance. Each dopant solution (1 mM) was measured at three different scan rates (1000, 500 and 100 mV/s) before and after addition of a ferrocene internal standard (also 1 mM). Data shown in Figure S1 are 100 mV/s scans except where noted; Figure S1a and S1b show measurements without and with Fc, respectively. We note that the use of an internal standard is critical in these measurements, as we observed shifts in the Ag/Ag^+ reference potential by up to 200 mV between different dopants.[7]

Table S 1: Dopant redox potential and estimated LUMO level from CV

Material	$E_{1/2}$ vs. Fc/Fc^+ (V)	Est.LUMO (eV)	Notes
TBA CN6-CP	-0.07	-5.03	Deconvoluted from Fc/Fc^+
Fc PF_6	0	-5.1	
F4TCNQ	0.15	-5.25	
F6TCNNQ	0.23	-5.33	
PMA	0.32	-5.42	
$Mo(tfd)_3$	0.45	-5.55	Solubility <1 mM in AN. $E_{1/2}$ extracted by inflection point method
$Mo(tfd\text{-}COCF_3)_3$	0.50	-5.60	Second redox wave deconvoluted from Fc/Fc^+
$Cu(OTf)_2$	0.63	-5.73	No transition visible after addition of Fc; calculated from $E_{1/2}$ before addition of Fc
CAN	0.67	-5.77	
CN6-CP	0.77	-5.87	Solubility ∼1 mM in AN. Second transition deconvoluted from Fc/Fc^+
$FeCl_3$	0.80 ± 0.08	-5.89 ± 0.08	See discussion in Section 2.2.2; $E_{1/2}$ extracted by inflection point method
OA	0.93	-6.03	Extremely unstable towards dilute water impurities

Table S1 shows the extracted redox potential for each dopant obtained from the measurements with Fc internal standard. We also provide the estimated LUMO level assuming a linear extrapolation from Fc/Fc^+ at -5.1 eV vs vacuum, as suggested by Cardona *et al.*[8] We stress that these LUMO levels should only be treated as an estimate; recent work has suggested that the relationship between $E_{1/2}$ and electron affinity is not necessarily linear,[9] and that $E_{1/2}$ is better correlated with the doping response because of shifts due to host environment.[6,10] In the context of ion exchange doping, the LUMO level is in any case less relevant than the $E_{1/2}$, as discussed in Section 1.3.

In several samples, the redox potential was not easily extracted using the standard $(E_{p,c} + E_{p,a})/2$ method,[11] either because the current was quite small, or because the redox wave was not fully reversible. In these cases (noted in Table S1) we used the inflection point to estimate $E_{1/2}$, as recently suggested by Espinoza *et al.*[12] An example of this extraction method is shown for $FeCl_3$ in Section 2.2.2.

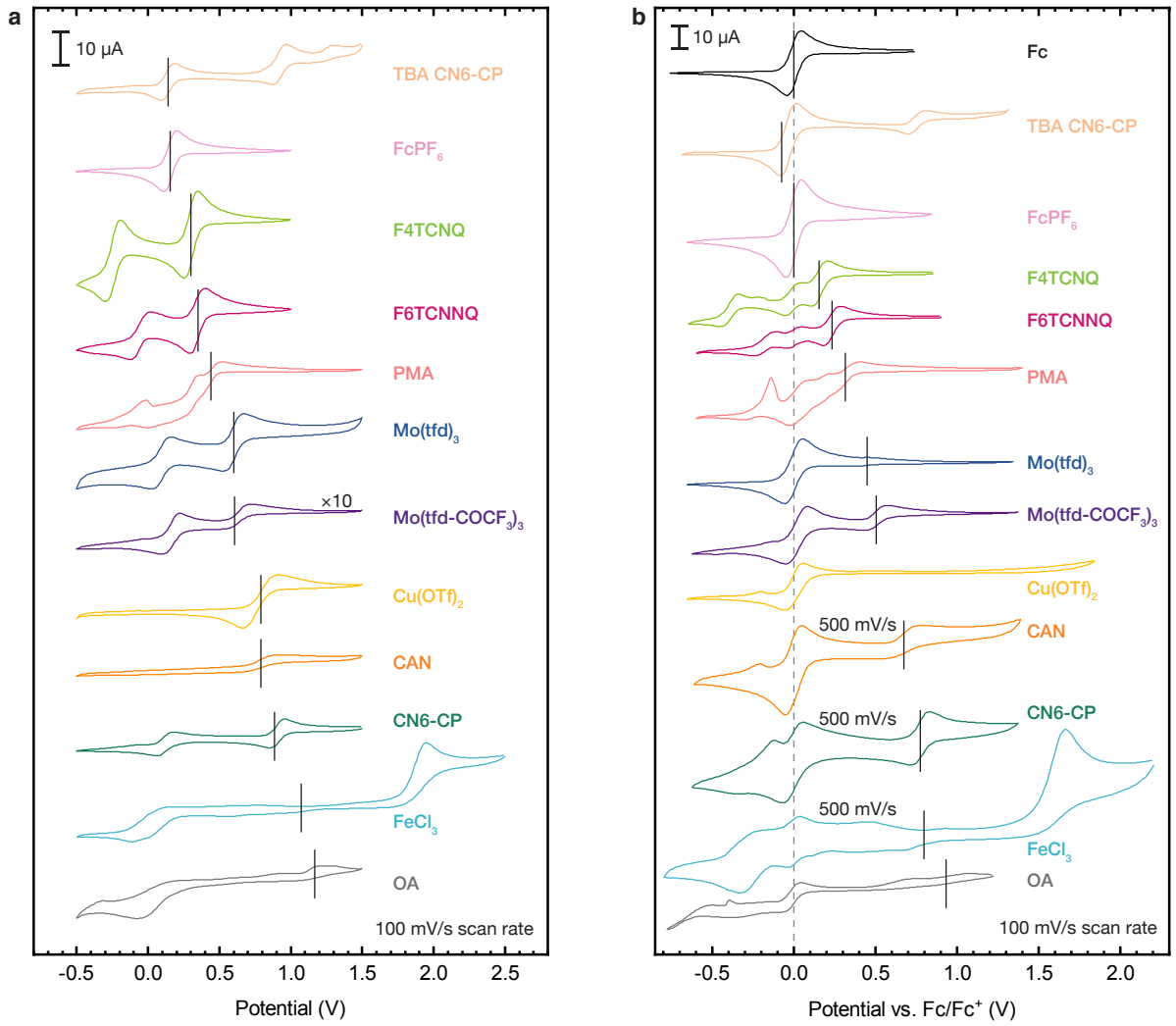

Figure S1: **Measurement of dopant strength using cyclic voltammetry** a) CV measurements of dopants (1 mM) in BMP TFSI (100 mM); potential is referenced to Ag/Ag^+. b) Measurement of each solution after addition of 1mM ferrocene as an internal standard. Potentials are referenced to Fc/Fc^+ at 0 V. Black lines in both plots indicate the extracted dopant redox potential.

2.2 Behavior of $FeCl_3$ in acetonitrile

2.2.1 Solution equilibrium

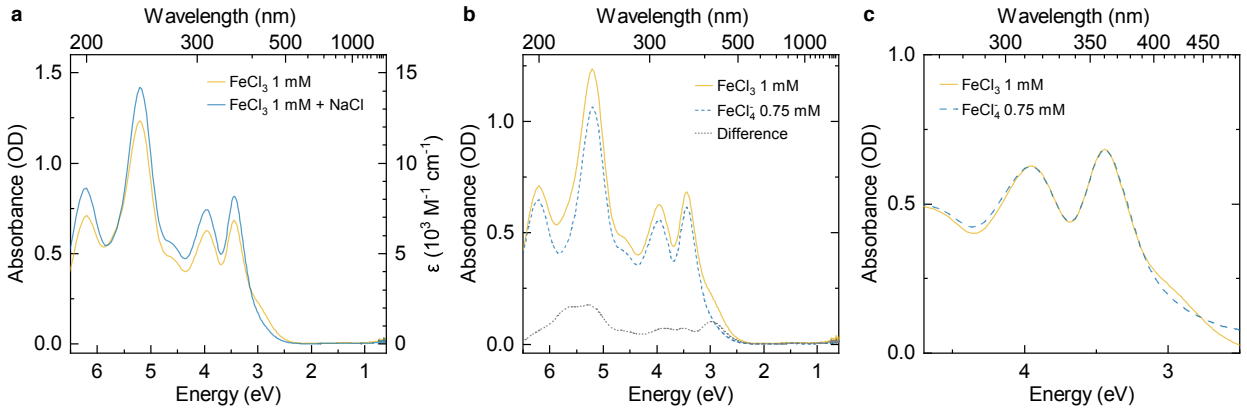

Figure S2: **Spectra of $FeCl_3$ solutions** a) UV-vis-NIR spectra of a $FeCl_3$ (1 mM in AN, anhydrous), and the same solution with excess NaCl added. Spectra were taken in 1 mm path length quartz cuvettes sealed under N_2; AN and cuvette background have been subtracted. Right axis shows the calculated molar absorptivity (ϵ). b) $FeCl_3$ solution spectrum and 0.75 mM $FeCl_4^-$ spectrum (obtained by scaling 1 mM $FeCl_3$ + NaCl spectrum). Gray dashed line shows the difference spectrum, which is consistent with Fe^{3+} cations.[13] c) Detail of 2.5 - 4 eV region of (b) with the 0.75 mM $FeCl_4^-$ fit offset vertically to illustrate that the amplitude of the spectral features are consistent.

Figure S2a (yellow line) shows a spectrum of an anhydrous 1 mM $FeCl_3$ / acetonitrile (AN) solution (also shown in Figure 3a, main paper). As discussed in the text, this spectrum indicates formation of the $FeCl_4^-$ anion[14,15] by a disproportionation mechanism:

$$[FeCl_4]^- \rightleftharpoons FeCl_3 \rightleftharpoons [FeCl_2]^+ \rightleftharpoons [FeCl]^{2+} \rightleftharpoons Fe^{3+} \tag{20}$$

We can shift the above equilibrium to the left by adding excess Cl^- ions in the form of NaCl. As shown by Liu et al, at high chloride concentrations, all iron in solution is converted to $FeCl_4^-$.[13] In the spectrum with added NaCl (Figure S2, blue line) we see enhanced absorption of the same peaks reported in as $FeCl_4^-$ in Swanson *et al.*, along with a reduced absorption of the shoulder around 3 eV. The peaks at 3.2 and 3.9 eV are also visible in $FeCl_3$ doped films without ion exchange, but are not present in most ion exchanged films. Therefore, we can confidently assign $FeCl_4^-$ as the counter-ion in non-ion exchange $FeCl_3$ doped films.

As discussed in the main text, the maximum $FeCl_4^-$ concentration that can be produced by disproportionation is 0.75 mM, corresponding to the reaction $4\,FeCl_3 \longrightarrow Fe^{3+} + 3\,[FeCl_4]^-$. Figure S2b shows the $FeCl_3$ solution spectrum overlaid with a $FeCl_4^-$ spectrum (simply the $FeCl_3$ spectrum with excess chloride shown in Figure S2a) scaled to a concentration of 0.75 mM. The difference between these two spectra is strictly positive and shows good agreement with published Fe^3+ spectra.[13] Furthermore, Figure S2c shows a detail of the fit in 2.5 - 4 eV region, with the $FeCl_4^-$ fit shifted up slightly to show that the amplitude of the spectral features match. Although not completely quantitative, these two observations suggest that the $FeCl_4^-$ concentration is roughly 0.75 mM, and therefore that in anyhdrous AN, $FeCl_3$ almost completely dissociates to Fe^{3+} and $FeCl_4^-$.

2.2.2 Fe^{3+} redox potential

Fe^{3+} was reported to show a very large redox potential difference between AN and water,[16] suggesting that the presence of even dilute water impurities should strongly affect the redox potential of our dopant

solutions. In solutions with water concentration on the order of that of the iron cation (∼100 ppm v/v) Kratochvil reports the reduction potential dropped from 1.57 V to 1.1 V,[16] vs. $AgNO_3$. This strong shift in potential is inconsistent with the prediction of the Nernst equation (59 mV / decade). To achieve such a significant reduction in redox potential, the Fe^{3+} concentration would need to be reduced by 8 orders of magnitude, at which point the concentration would be too low for the redox reaction to be observed.

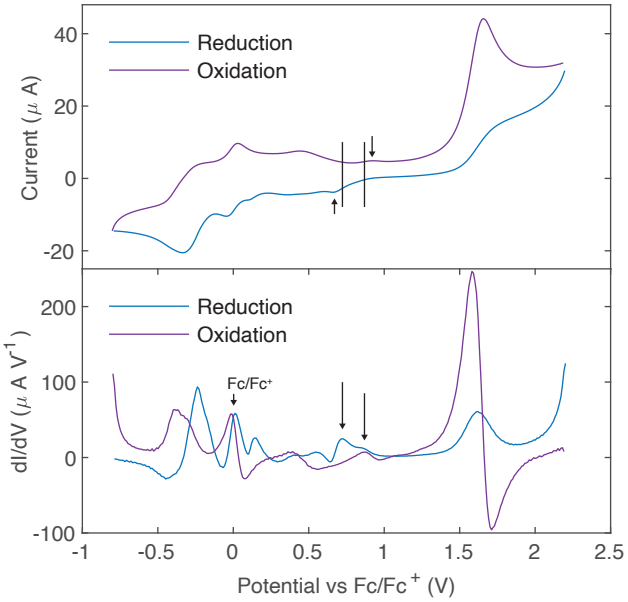

Figure S3: **Redox potential extraction in $FeCl_3$ by inflection point method** a) CV measurements of $FeCl_3$ (1 mM) in BMP TFSI (100 mM). Scan rate is 500 mV/s, potential is referenced to internal Fc/Fc^+ standard (1 mM). b) Data in (a) replotted as dI/dV. Redox waves assigned to Fe^{3+}/Fe^{2+} are indicated by arrows.

Our CV data, which includes an intrinsic water impurity of at least ∼100 μM (∼10 mol% vs. $FeCl_3$), agrees well with the literature value for lightly hydrated $FeCl_3$. In our data (Figure S3a) we observe several redox waves, consistent with the disproportionation behavior observed in $FeCl_3$ solutions (Figure S3a). The highest observed redox wave, at about 1.5 V vs. Fc/Fc^+, shows irreversible oxidation behavior and is therefore assigned to oxidation of chloride ligands to free chlorine, i.e. $FeCl_4^- \longrightarrow FeCl_3 + Cl + e^-$. The next highest redox wave is observed at about 0.8 V vs Fc/Fc^+ and shows partially reversible behavior; this is the wave is responsible for the doping behavior of $FeCl_3$ solutions. The potential of this wave varied slightly between measurements on different days, indicating that the change in redox potential is not due to a reaction with e.g. OH^- ions, but rather due to a homogenous shift in the $Fe^{3+} \longleftrightarrow Fe^{2+}$ potential.

Additional weak features observed in the CV at lower potentials are consistent with reduction of various ligand-deficient Fe(iii) to Fe(ii) species which form as the solution redox potential is swept. In this context we can assign lowest redox wave, previously reported by Liang *et al.*,[17] to the reduction of $FeCl_4^-$, i.e. $FeCl_4^- + e^- \longleftrightarrow FeCl_4^{2-}$.

The low intensity of peaks in the CV data, resulting from the relatively low concentration of Fe^{3+}, make direct determination of $E_{1/2}$ somewhat ambiguous. Instead, we use a new approach to estimate the redox potential proposed by Espinoza *et al.*[12] Figure S3b shows this method. The CV data (Figure S3a) is replotted as dI/dV (Figure S3b); the redox potential in partially or fully irreversible waves is then obtained from these peaks. As a conservative estimate of the redox potential for $FeCl_3$, we use the reduction potential obtained from the peak at 0.73 V (left arrow in Figure S3b) rather than the weak shoulder near the oxidation

potential at 0.88 V. Thus, we obtain 0.8 ± 0.08 V for $E_{1/2}$, where the uncertainty arises from the ambiguity observed in the reduction sweep. The value obtained from the inflection point method is in good agreement with the $E_{1/2}$ obtained from the average of the peak potentials (arrows in Figure S3a), giving us confidence in our estimate of $E_{1/2}$. Even using this slightly conservative estimation of $E_{1/2}$, the redox potential of $FeCl_3$ is still higher than any reported organic dopant molecule,[18] and explains the extremely strong doping response we observe with $FeCl_3$ / AN solutions.

2.3 Behavior of CN6-CP in acetonitrile

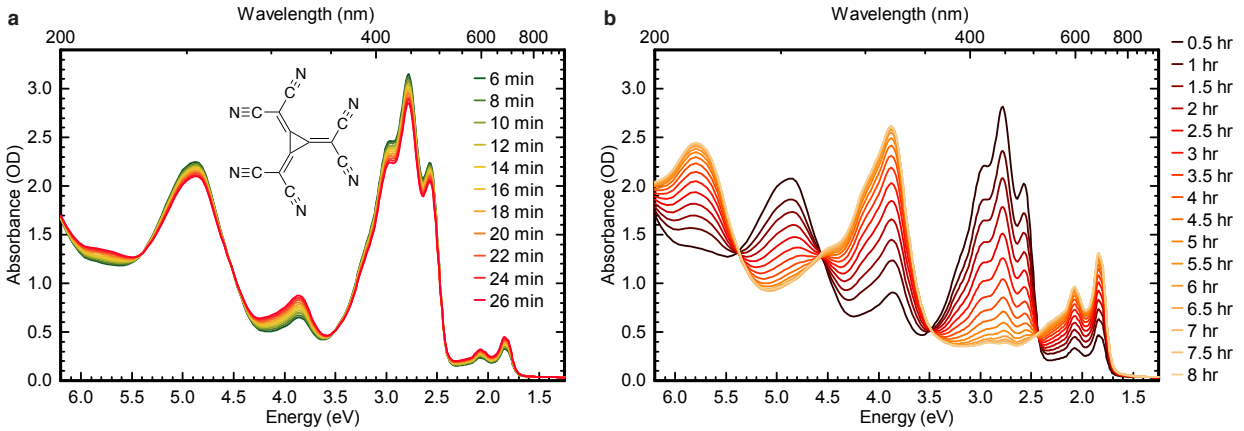

Figure S 4: **UV-vis spectra of CN6-CP solutions** a) CN6-CP solution in AN (0.2 mg/mL) measured in quartz cuvette (1 mm pathlength) sealed under N_2. Time shown indicates time since solution was prepared. b) Spectra of the same solution in (a) collected every half hour.

In the initial report of CN6-CP, the strongest organic molecular dopant reported to date, the authors were unable to identify a solvent in which the neutral molecule was both stable and soluble.[19] However, as shown in Figure S4, we find CN6-CP does appear to be sufficiently stable in dry acetonitrile for experimental work. Figure S4a shows spectra of a 0.2 mg/ml CN6-CP/AN solution taken two minutes apart; the time shown is counted from the time the solution was prepared. The peaks near 2 and 3.8 eV are consistent with those of the radical anion, CN6-$CP^{\bullet -}$, reported previously.[19] The features at 2.8 eV and 5 eV decrease with time to generate the radical anion and result in formation of clear isobestic points, indicating a simple X $\longrightarrow$ Y reaction. Therefore the absorbance at 2.8 eV and 5 eV must correspond to neutral CN6-CP. Stability in solution is generally poor; we observe a half-life of the neutral species of roughly 2 hours. However, we believe that the auto-ionization seen here is likely due to interaction with an impurity (e.g. water) and not the solvent itself, since acetonitrile is aprotic and has an electrochemical window that extends over a volt beyond the reduction potential of CN6-CP. In this case, the observed half-life may not be intrinsic, but rather related to the rate of moisture ingress into the sealed cuvette.

The tendency of CN6-CP to auto-ionize makes the solubility in acetonitrile difficult to measure because ionization tends to increase the solubility in polar solvents. Visually, we observe clear aggregates in solutions above 0.5 mg/mL but not at 0.2 mg/mL. Therefore, the 1 mM (0.228 mg/mL) solutions used in our ion exchange process appear to be near the solubility limit in AN.

2.4 A note on water stability

Both AN and the electrolytes studied here almost inevitably contain a small water impurity (10-20 ppm in AN, up to several ppt in some electrolytes; see Methods). From these values we estimate a water concen-

tration of 100s of μM in the doping solution. Together with the additional adsorbed water on the surfaces of vials and pipette tips, the total water concentration in the final doping solution is higher still, and likely approaches the dopant concentration (1 mM) in some of the wetter electrolytes. If the dopant displays a strong instability towards water, the effective dopant concentration may be significantly lower than 1 mM.

The strongest dopant we studied, OA (triethyloxonium hexachloroantimonate) was previously reported as an effective dopant for carbon nanotubes.[20] Unfortunately, OA is strongly unstable towards water, which makes it effectively incompatible with ion exchange doping. As a result, OA yields low conductivities (1.1 S/cm) upon ion exchange with PBTTT (100/1 mM BMP TFSI / OA, 100 sec), despite its ostensibly high reduction potential. We confirmed this mechanism by intentionally adding a small water impurity (1 ppt) to the doping solution, which yielded a conductivity comparable to undoped PBTTT (4×10^{-3} S/cm).

$FeCl_3$ is also to be sensitive to water, however this sensitivity appears to result in a continuous shift in the redox potential, as described in the preceding section.[16] For strong dopants such as $FeCl_3$, this is an acceptable situation, and may even be useful for tuning the redox strength to control the doping level. In any case, the strong water concentration dependence of the Fe^{3+} reduction potential places some limitations on the applicability of $FeCl_3$ for ion exchange: our results suggest that doping with $FeCl_3$ solutions in air is generally ineffective, and that $FeCl_3$ / AN solutions have a limited lifetime even in the glovebox. In addition, dry solvents and reagents ($FeCl_3$ and electrolytes) are generally required.

3 Exchange efficiency characterization

3.1 XPS measurements

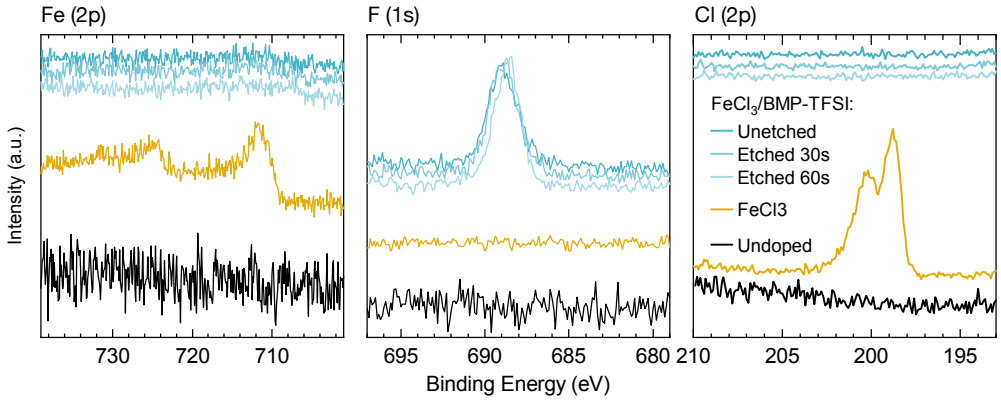

Figure S5: **Elemental analysis of ion exchange doped films with XPS**. XPS spectra of PBTTT thin films undoped, $FeCl_3$ (1 mM) doped, and BMP-TFSI / $FeCl_3$ (100 / 1 mM) doped, showing the Fe 2p edge, F 1s edge, and Cl 2p edge.

To verify the efficiency of our ion exchange process, we performed X-ray photoemission spectroscopy (XPS) measurements on a neat PBTTT film, a PBTTT film doped with $FeCl_3$, and a PBTTT film doped by ion exchange (100 / 1 mM BMP TFSI / $FeCl_3$). These results are shown in Figure S5. XPS spectra were collected on a Thermo Scientific Escalab 250xi, using a pass energy of 20 eV, step size of 0.1 eV, and spot size of 400 μm. 30 scans were collected for each spectrum. To minimize charging, films were prepared on gold electrodes and the flood gun was used.

As expected, we observe strong signals from both Fe and Cl in the $FeCl_3$ doped sample, while the BMP-TFSI / $FeCl_3$ ion exchange doped sample shows no signal for either. Instead, we see a strong F signal in the BMP-TFSI / $FeCl_3$ ion exchange sample, resulting from the $TFSI^-$ ions, which is not present in the $FeCl_3$ or undoped samples. XPS is a surface sensitive technique, so to ensure that ion exchange occurred within the bulk of the film, we additionally measured the BMP-TFSI / $FeCl_3$ spectra after etching with argon ions for 30 sec and 60 sec. The spectra of the etched ion exchange doped films do not vary with etching time, indicating that the film composition is uniform in the vertical direction, consistent with our UV-vis data (Figure 2, main paper).

3.2 Fitting residual $FeCl_4^-$ concentration spectroscopically

As shown in Figure S2, the $FeCl_4^-$ anion has several sharp absorption features in the UV. Two of these features, at 3.3 and 3.8 eV, are below the absorption edge of our glass substrates ($\sim$ 4.1 eV) and are visible in $FeCl_3$ doped films. We can use these features to estimate the $FeCl_4^-$ concentration in doped films by fitting these UV absorption features to a reference $FeCl_4^-$ spectrum.

To obtain the molar absorptivity of $FeCl_4^-$, we use the 1 mM $FeCl_3$ + excess NaCl spectrum in Figure S2 as a 1 mM $FeCl_4^-$ spectrum. As discussed previously, the addition of excess chloride converts $FeCl_3$ to $FeCl_4^-$. The $FeCl_4^-$ molar absorptivity ϵ can be determined from the absorption spectrum using the Beer-Lambert Law,

$$\epsilon(E) = \frac{A(E)}{lc} \tag{21}$$

Table S 2: $FeCl_4^-$ UV spectral fit details

Figure	Polymer	Sample set	Fit range (eV)	Baseline function	δ range (eV)
Figure S6	PBTTT	Electrolyte conc. dep.	$2.8 < E < 4.3$	Poly. (3rd order)	$-0.07 < \delta < -0.06$
Figure S7	PBTTT	$FeCl_3$ conc. dep.	$2.8 < E < 4.3$	Poly. (3rd order) + Undoped spectrum	$-0.07 < \delta < -0.06$
Figure S8	PBTTT	BMP TFSI time-dep.	$2.8 < E < 4.3$	Poly. (3rd order) + Undoped spectrum	$-0.07 < \delta < -0.06$
Figure S9	P3HT	TBA PF_6 time-dep.	$2.8 < E < 4.3$	Poly. (3rd order) + Undoped spectrum	$-0.10 < \delta < -0.09$

where $\epsilon(E)$ and $A(E)$ is the molar absorptivity and absorbance, respectively, at energy E, l is the cuvette path length (1 mm), and c is the $FeCl_4^-$ concentration (1 mM). We then fit the UV absorption region of the thin films to the sum of the anion absorption plus a baseline function $B(E)$:

$$A(E) = \epsilon(E - \delta) l_f c + B(E) \tag{22}$$

where l_f is the film thickness. To obtain good fits we find it is necessary to include a solvatochromic shift, δ, which arises because the dielectric constant of the polymer ($\epsilon \sim 3$) is much lower than AN ($\epsilon = 39$). Solvatochromism is common in metal-centered inorganic and organometallic compounds because metal-ligand bonds have significant charge transfer (CT) character, and CT state energies are strongly affected by the dielectric constant of their environment.[21] For each polymer, δ was first obtained by fitting the spectrum of a pure $FeCl_3$ doped film, then restricted to a small range for the ion exchange doped samples to prevent overfitting.

The baseline function and fit range depend on the polymer; see Table S2 for details. In general, the function was a polynomial function, plus the undoped polymer absorption spectrum in series where fits covered a range of doping levels:

$$B(E) = \sum_{i=0}^{n} c_i E^i + c_u A_u(E) \tag{23}$$

where c_i are fit coefficients and $A_u(E)$ is the undoped polymer absorption. In the fully doped PBTTT and P3HT spectra, our fitting routine did not assign any weight to the undoped polymer spectrum, as expected.

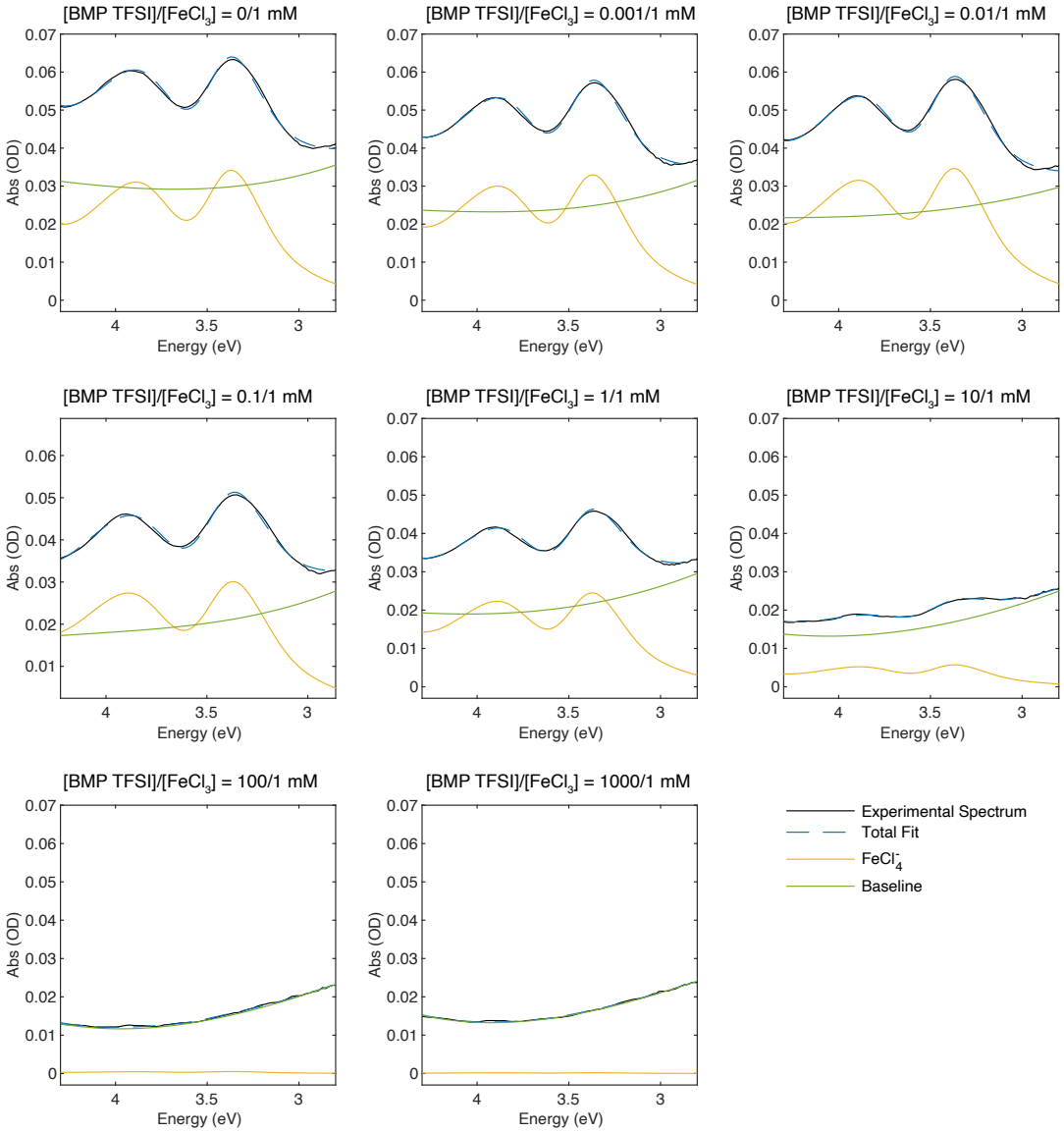

Figure S6: **PBTTT/$FeCl_3$/BMP-TFSI electrolyte concentration dependent UV fits**. Fits to UV-vis spectra of ion exchange doped PBTTT films. Doping solutions contained 1 mM $FeCl_3$ with variable BMP-TFSI electrolyte concentration (see label above each plot); exposure time was 100 sec. For fit details see Table S2.

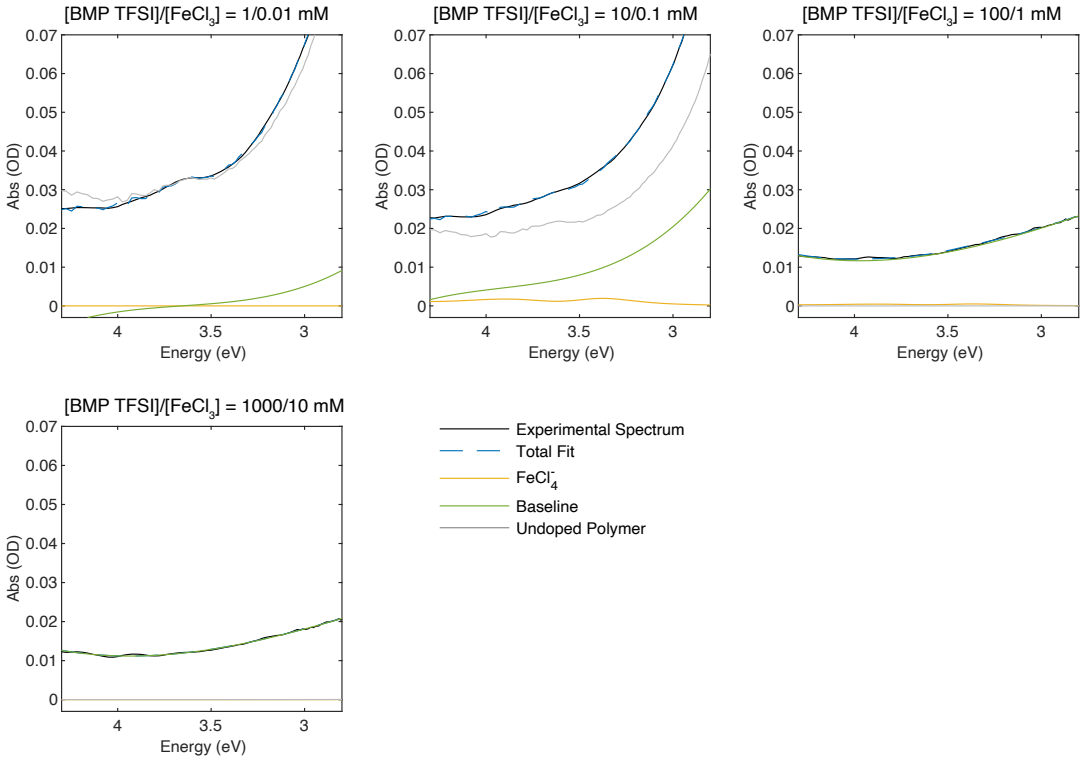

Figure S7: **PBTTT/$FeCl_3$/BMP-TFSI dopant concentration dependent UV fits**. Fits to UV-vis spectra of ion exchange doped PBTTT films. Doping solutions contained varying concentrations of $FeCl_3$ with a 100-fold excess of BMP-TFSI (see label above each plot); exposure time was 100 sec. For fit details see Table S2.

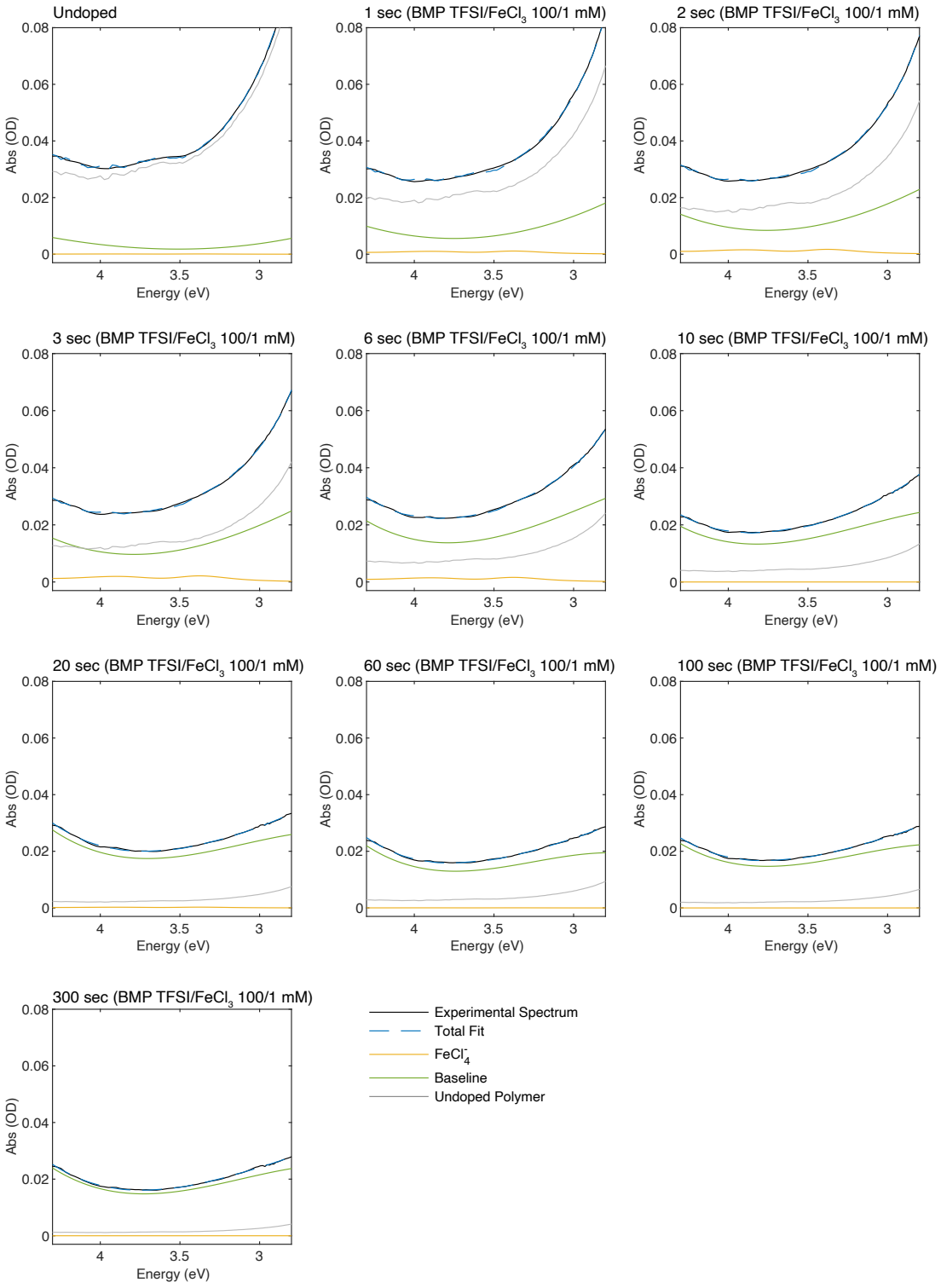

Figure S8: **PBTTT : BMP TFSI UV-vis fits, variable doping time**. Fits to UV-vis spectra of ion exchange doped PBTTT films. Doping solutions contained 1 mM $FeCl_3$ and 100 mM BMP-TFSI (see label above each plot); exposure time was varied. For fit details see Table S2.

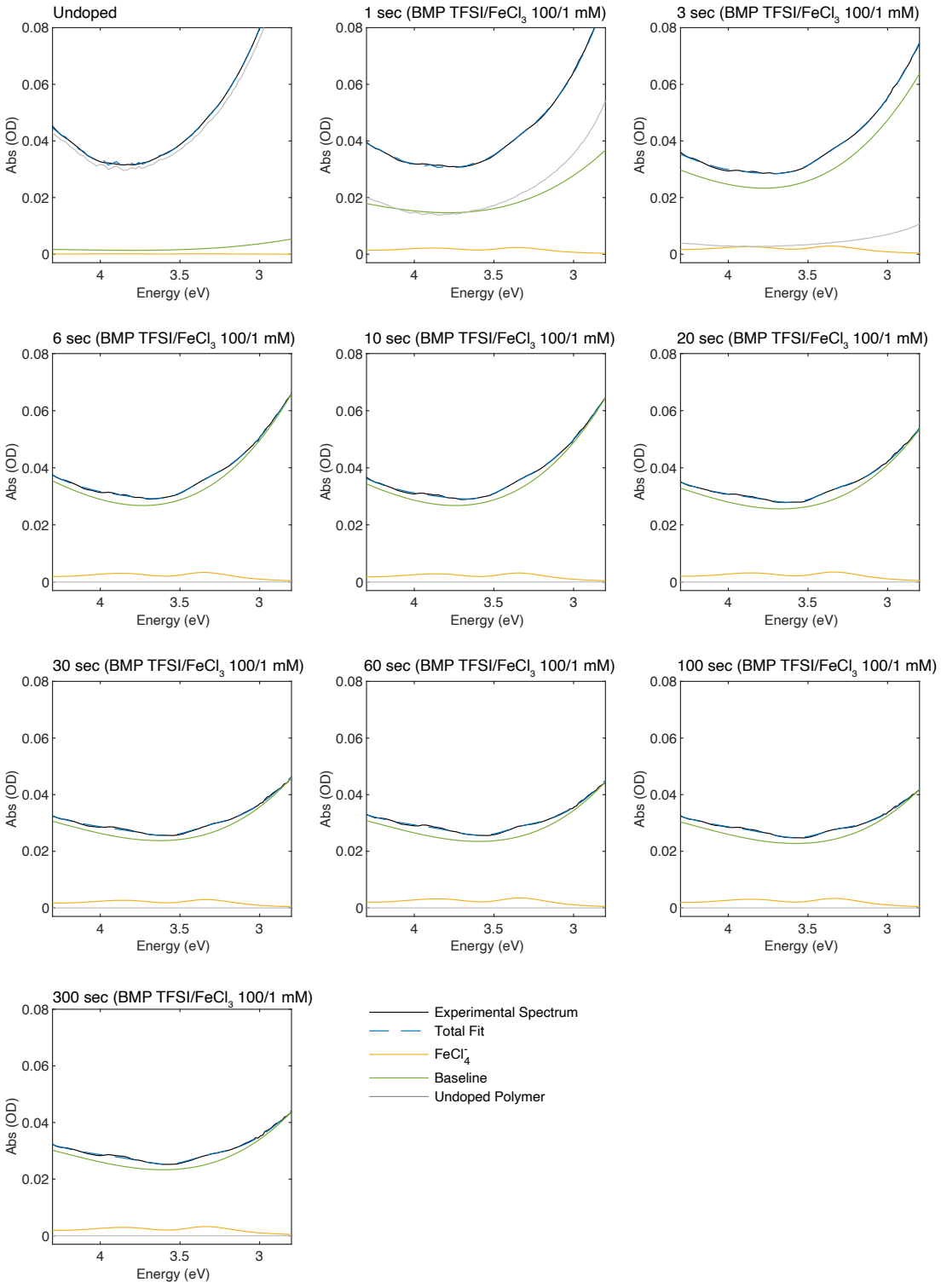

Figure S9: **P3HT : TBA PF_6 UV-vis fits, variable doping time**. Fits to UV-vis spectra of ion exchange doped P3HT films. Doping solutions contained 1 mM $FeCl_3$ and 100 mM TBA PF_6 (see label above each plot); exposure time was varied. For fit details see Table S2.

3.3 Exchange efficiency with other dopants

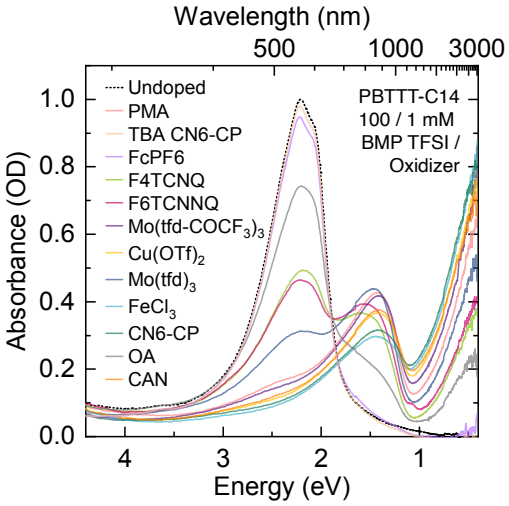

Figure S10: **UV-vis-NIR spectra of PBTTT films shown in Figure 3, main paper**. UV-vis-NIR spectra of PBTTT ion exchange doped with BMP TFSI (100 mM) plus different dopants (1 mM) in AN. Doping time was 100 seconds.

Tables S3 and 4 show the expected absorption bands and molar absorptivity for each relevant redox state of the dopants studied in Figure 3 of the main paper. Figure S10 shows the UV-vis-NIR spectra of the samples shown in Figure 3 of the main paper: PBTTT films doped using 100:1 mM BMP-TFSI:dopant solutions. With the exception of a small peak in the F6TCNNQ spectrum, we do not observe any spectral features corresponding to the reduced dopant ions, indicating that ion exchange exchange efficiency is high for all samples. The feature observed in F6TCNNQ, at 1.1 eV, corresponds to a very strong transition in the F6TCNNQ$^{\bullet-}$ anion ($\epsilon = 5.3 \times 10^4$ M^{-1} cm^{-1}). Based on the measured absorbance in the F6TCNNQ ion exchange doped film, we estimate a residual F6TCNNQ$^{\bullet-}$ concentration of about $1{\times}10^{19}$ cm^{-1}. This value is similar to the residual $FeCl_4^-$ concentration observed with $FeCl_3$ doping (Figure 2b, main paper). We speculate that this impurity could result from kinetically trapped F6TCNNQ$^{\bullet-}$ ions, or residue of the BMP F6TCNNQ$^{\bullet-}$ ion exchange product on the surface of the film.

This universally high exchange efficiency observed here is in line with our expectations: $FeCl_4^-$ has both smallest size of all the oxidation products studied, and disproportionates in solution to yield a high concentration of $FeCl_4^-$, (i.e. $C_{D,s}^-$ in Equation S11). Both of these factors should reduce exchange efficiency, yet as shown in Figure 2b of the main paper, this system still yields an exchange efficiency of >98%.

Table S 3: Absorption bands of neutral and reduced dopant molecules

Material	λ_{max} (eV)	ϵ (M^{-1} cm^{-1})	Notes	Reference
Ferrocene	2.81	87	in isooctane	Ref. 22
	3.81	51	in isooctane	Ref. 22
	5.1	2.5×10^3	in isooctane	Ref. 22
F4TCNQ	3.2	73×10^3	in CH_3CN	Ref. 23
$F4TCNQ^{\bullet-}$	1.45	42×10^3	in CH_3CN	Refs. 23,24
	1.65	20×10^3		
	1.81	5.7×10^3		
	3.02	49×10^3		
$F4TCNQ^{2-}$	3.8	28×10^3	in CH_3CN	Ref. 23
F6TCNNQ	2.57	Similar to F4TCNQ	in CH_3CN	Refs. 25,26
$F6TCNNQ^{\bullet-}$	1.08	53.7×10^3	in CH_3CN	Refs. 25,26
	1.27	23×10^3		
	2.1	–		
	2.2	–		
	3.1	–		
PMA^{3-}	4	–	in n-butyl acetate	Ref. 27
PMA^{5-}	$\sim$ 1.5, broad	–	in water/dioxane	Ref. 28
$Mo(tfd)_3$	2.13	11×10^3	in CH_2Cl_2	Ref. 29
	3.21	8.5×10^3		
$Mo(tfd)_3^{\bullet-}$	1.9	Sim. to $Mo(tfd\text{-}COCF_3)_3^{\bullet-}$	in CH_2Cl_2	Ref. 30
	2.5		ϵ not reported	
	3.2			
$Mo(tfd)_3^{2-}$	–	–	Not reported, presumably simliar to $Mo(tfd\text{-}COCF_3)_3{}^{2-}$	Ref. 29,31

Table S 4: Absorption bands of reduced dopant molecules (continued)

Material	λ_{max} (eV)	ϵ (M^{-1} cm^{-1})	Notes	Reference
$Mo(tfd\text{-}COCF_3)_3$	2.1	13×10^3	in CH_2Cl_2	Ref. 29
	3.0	10×10^3		
$Mo(tfd\text{-}COCF_3)_3^{\bullet-}$	1.9	4×10^3	in CH_2Cl_2	Ref. 29
	2.5	2×10^3		
	3.2	4×10^3		
$Mo(tfd\text{-}COCF_3)_3^{2-}$	1.9	5×10^3	in CH_2Cl_2	Ref. 29
	4	2×10^3		
	∼3.5	$\sim10\times10^3$		
Cu^{2+} ($Cu(OTf)_2$)	1.29	–	as nujol mull	Ref. 32
OTf^-	>6	–		
Ce^{4+} (CAN)	3.87	3.1×10^3	in conc. H_2SO_4	Ref. 33
Ce^{3+} (CAN)	4.35	240	in conc. H_2SO_4	Ref. 33
	4.96	1×10^3		
	5.16	1×10^3		
CN6-CP	2.58	25×10^3	in CH_3CN	This work, Figure S4
	2.79	35×10^3		
	2.96	28×10^3		
	4.88	25×10^3		
$CN6\text{-}CP^{\bullet-}$	1.82	15×10^3	in CH_3CN	This work, Figure S4,
	2.08	12×10^3		also see Ref. 19
	3.88	30×10^3		
	5.7	28×10^3		
$CN6\text{-}CP^{2-}$	3.93	33.4×10^3	in CH_3CN	Ref. 34
	4.35	22×10^3		
	5.59	35.8×10^3		
$FeCl_3$	3.3	5.5×10^3	in EtOH	Ref. 14
	5.1	8×10^3		
$FeCl_4^-$	3.44	8.1×10^3	in AN	this work, Figure S2, also ref. 14
	3.96	7.4×10^3		
	5.21	14.2×10^3		

4 Full GIWAXS results

Full GIWAXS results are give below; data processing details are located in the main paper methods section.

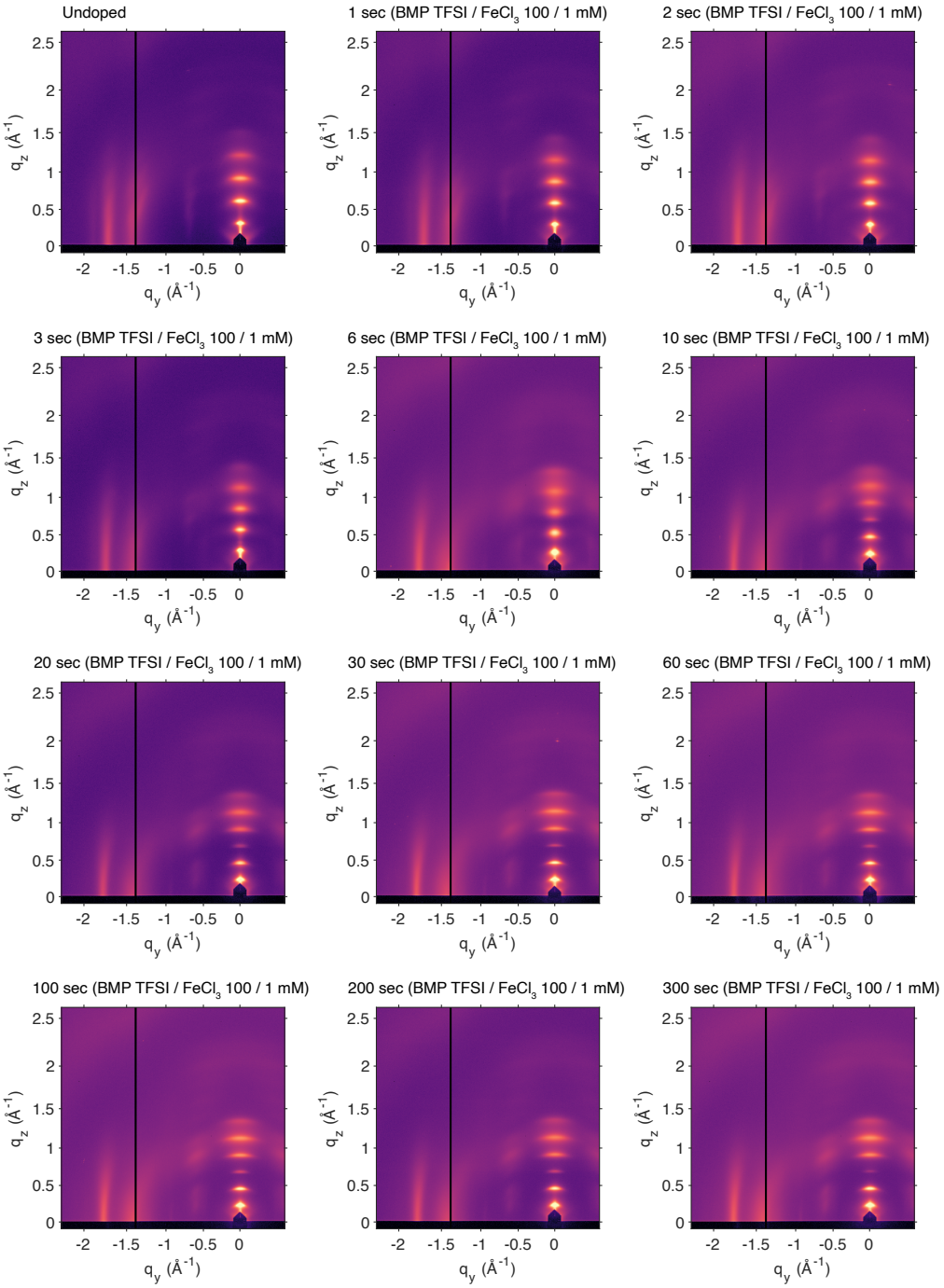

Figure S11: **PBTTT : BMP TFSI GIWAXS patterns, variable doping time**. Doping solutions contained 1 mM $FeCl_3$ and 100 mM BMP-TFSI (see label above each plot); exposure time was varied.

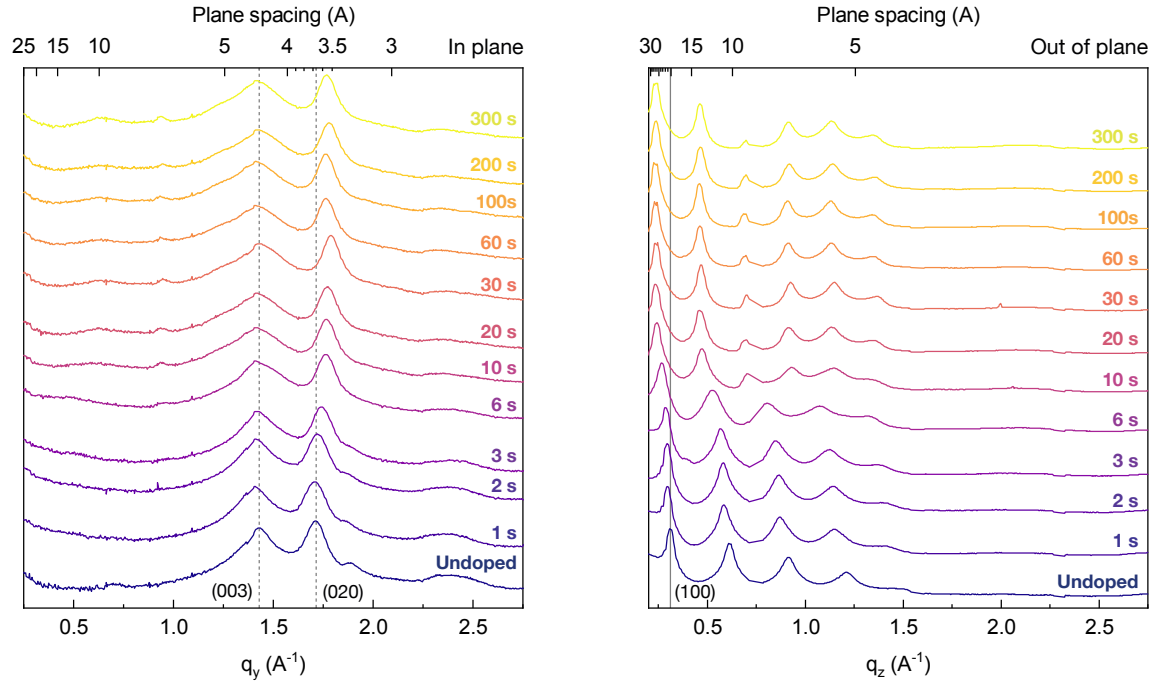

Figure S12: **PBTTT : BMP TFSI GIWAXS linecuts, variable doping time**. Doping solutions contained 1 mM $FeCl_3$ and 100 mM BMP-TFSI (see label above each plot); exposure time was varied.

Table S 5: Lattice spacings and paracrystallinity extracted from PBTTT GIWAXS data

Doping time	q_{lam}	d_{lam}	$q_{\pi-\pi}$	$d_{\pi-\pi}$	$g_{\pi-\pi}$
Undoped	0.310	20.24	1.712	3.67	9.41
1 s	0.296	21.22	1.708	3.68	9.63
2 s	0.295	21.33	1.722	3.65	9.47
3 s	0.288	21.83	1.742	3.61	9.42
6 s	0.267	23.55	1.762	3.57	8.75
10 s	0.242	26.00	1.766	3.56	8.71
20 s	0.236	26.63	1.771	3.55	8.96
30 s	0.239	26.32	1.788	3.51	8.55
60 s	0.235	26.71	1.764	3.56	9.02
100 s	0.234	26.87	1.763	3.56	8.44
200 s	0.237	26.50	1.778	3.53	8.68
300 s	0.237	26.54	1.767	3.56	8.44

5 Dopant concentration dependence

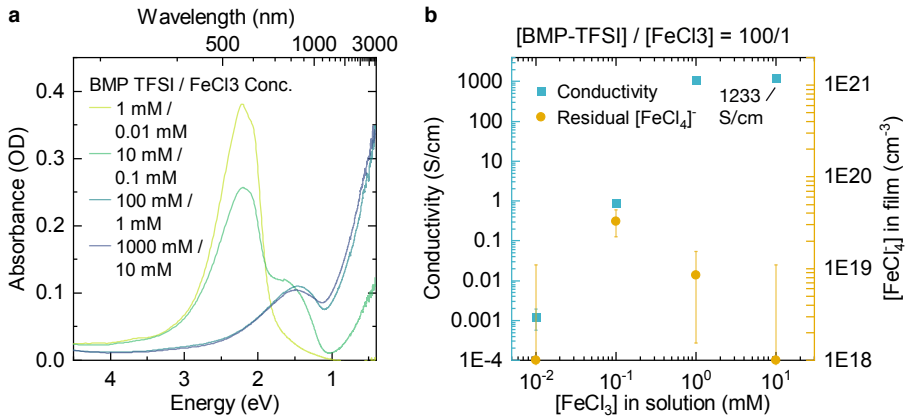

Figure S 13: **Controlling doping level via $FeCl_3$ concentration**. a) UV-vis-NIR spectra of PBTTT films doped at a fixed 100:1 BMP TFSI : $FeCl_3$ mole ratio with variable total concentration; doping time was 100 s. I) Conductivity (blue squares) and residual $FeCl_4^-$ concentration (yellow circles) for films shown in (a).

In sequential doping processes such as the ion exchange process explored here, the doping level is typically controlled by varying the concentration of the dopant solution, which in reversible processes controls the equilibrium via the Langmuir isotherm (Section 1). Figure S13 shows UV-vis, conductivity, and exchange efficiency for PBTTT films ion exchange doped with varying $FeCl_3$ concentration. The electrolyte concentration was fixed at 100 times the $FeCl_3$ concentration. We observe a sharp drop off in doping level for $FeCl_3$ concentrations below 1 mM. Interestingly, ion exchange efficiency also drops at lower $FeCl_3$ concentrations. This drop off in exchange efficiency appears to be driven by a structural phase transition, as discussed in the main text.

At high $FeCl_3$ concentration (10 mM) conductivity and exchange efficiency both increase modestly, allowing for conductivity in excess of 1200 S/cm and ion exchange efficiencies too high to measure spectroscopically. However, these concentrated solutions are also extremely corrosive; we observed that 1000/10 mM BMP TFSI / $FeCl_3$ solution were able to fully etch unprotected gold contacts in under a minute. This property limits the applicability of these high concentrations for device applications. The 100/1 mM electrolyte/dopant concentration used in our study therefore does not provide the maximum doping level possible, but rather represents a compromise between reaching high carrier densities and allowing for systematic study of many material combinations.

6 Ion exchange kinetics in P3HT

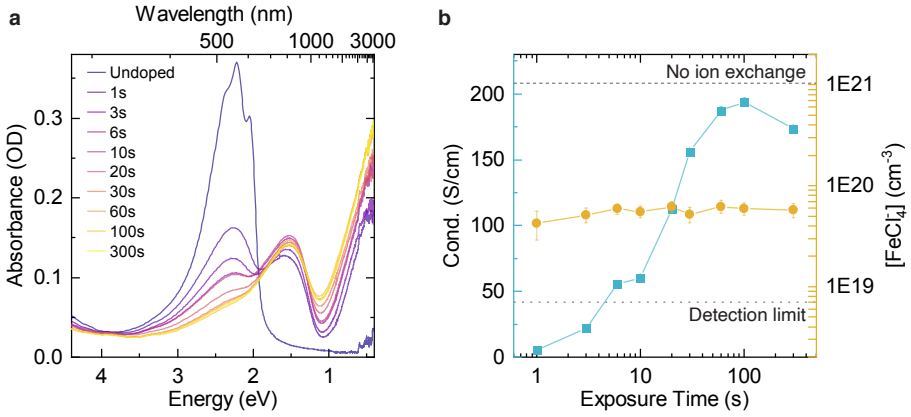

Figure S14: **P3HT doping time dependent UV-vis, conductivity, and exchange efficiency** Doping solutions consisted of 100 /1 mM TBA PF_6 / $FeCl_3$ in AN. a) UV-vis-NIR spectra. b) Electrical conductivity and residual $FeCl_4^-$, extracted from UV-vis spectra.

The kinetics of P3HT doping, in contrast to PBTTT, are relatively straightforward. We studied ion exchange kinetics in TBA PF_6 / $FeCl_3$, the electrolyte which gave the highest conductivity in P3HT (full details of the role of ion size will be published separately). The UV-vis spectra (Figure S14a) shows the doping process reaches equilibrium at about 60 seconds, with only a small degree of P2 bleaching at long doping times. Electrical conductivity peaks at 100 seconds before dropping slightly at 5 minutes. The peak conductivity observed here is similar to that recently reported by Neusser *et al.* (223 S/cm) in P3HT:PF6 prepared electrochemically.[35]

Surprisingly, the residual $FeCl_4^-$ concentration is only weakly time-dependent in P3HT:PF_6 (Figure S14b). As will be discussed in an upcoming work, PF_6 generally shows lower exchange than TFSI, which is likely due to a hydration shell formed by water impurities.[36] The time independence of residual $FeCl_4$ is therefore indicative of a fairly large, positive ΔG^0_{ex}, at least for a ions in some portion of the microstructure, resulting from this hydration shell.

7 Stability of doped films

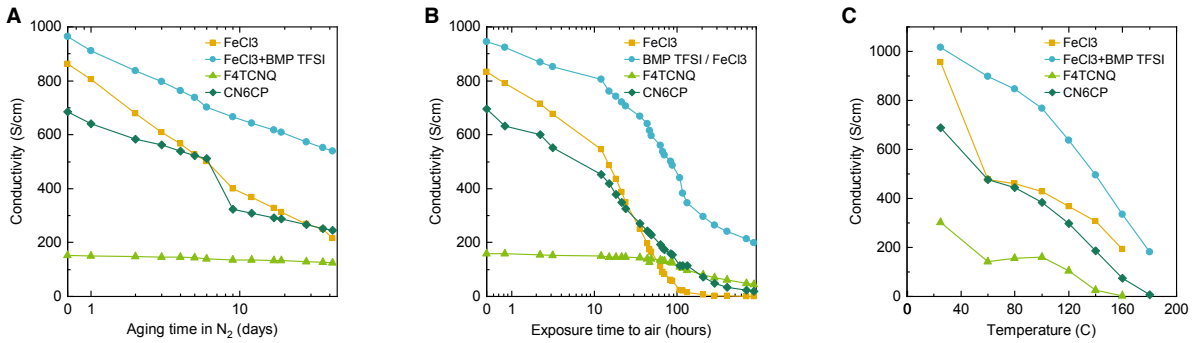

Figure S15: **Stability of PBTTT doped via ion exchange and molecular dopants**. Conductivity of PBTTT films stored under nitrogen (a) and air (b) vs. aging time. c) Thermal stability of PBTTT films heated to progressively higher temperatures; hold time at each temperature was 10 minutes.

As discussed in the introduction of the main paper, a potentially major advantage of ion exchange is the prospect of improved doped film stability. Previous works on ion exchange doping have shown improvements in ambient and thermal stability in doped PBTTT.[37,38] Our device stability measurements, shown in Figure S15, largely confirm these previous results. Nonetheless, both the residual air instability and thermal stability are somewhat puzzling. Most molecular dopants, including F4TCNQ and CN6-CP, dope via reversible charge transfer. Neutral F4TCNQ and CN6-CP have non-negligible vapor pressure at elevated temperatures, therefore we expect dopant neutralization followed by sublimation out of the film to be a major cause of thermal instability in these systems. The HOMO of TFSI, on the other hand, is multiple eV deeper than the PBTTT polaron band, therefore reverse electron transfer is very energetically unfavorable. We would therefore expect ion exchange doping to dramatically improve doped film thermal stability by shutting off this dedoping mechanism. The fact that the thermal stability is not further improved, though disappointing, nonetheless suggests something quite interesting: many of the instabilities in doped polymers often attributed to unstable dopants may in fact be intrinsic instabilities of the polymer themselves. This conclusion echos the results of Figure 5, main paper.

TFSI based ionic liquids are typically thermally stable to temperatures in excess of 400°C.[39] Since in the presence of a stable cation the TFSI anion should be thermally stable to temperatures well above those studied here, the drop in conductivity with thermal stress suggests that PBTTT polarons may themselves be unstable. The origin of this residual instability is unclear, but as we observe partial recovery of the polymer $\pi - \pi^*$ band after thermal stress or extended exposure to air, some reaction leading to reduction of PBTTT polarons to neutral PBTTT (i.e. dedoping) must be occuring. As seen in Figure 4 of the main paper, even a small residual $\pi - \pi^*$ absorbance is associated with much lower conductivity, therefore the dedoping visible by eye in these samples is likely sufficient to explain the drop in conductivity. This process could involve dilute water impurities, e.g. donation of charge from hydroxide ions, or an intramolecular redox reaction leading to a cation localized on the polymer. However, we stress that given the electronic structure of TFSI, simple reverse charge transfer followed by sublimation of TFSI out of the film is rather implausible. Similarly, formation of fractional CTCs via slow structural evolution as recently reported for P3HT:F4TCNQ[40]—is less likely here. Due to the absence of TFSI electronic states in the energetic vicinity of the PBTTT HOMO, fractional CTCs, which are responsible for the drop in conductivity observed by Watts *et al.*, should not be possible with TFSI. However, given the importance of air stability to industrial application of these materials, characterization of these mechanisms and identification of stabilization methods remains critical, despite the improvements made possible by ion exchange.

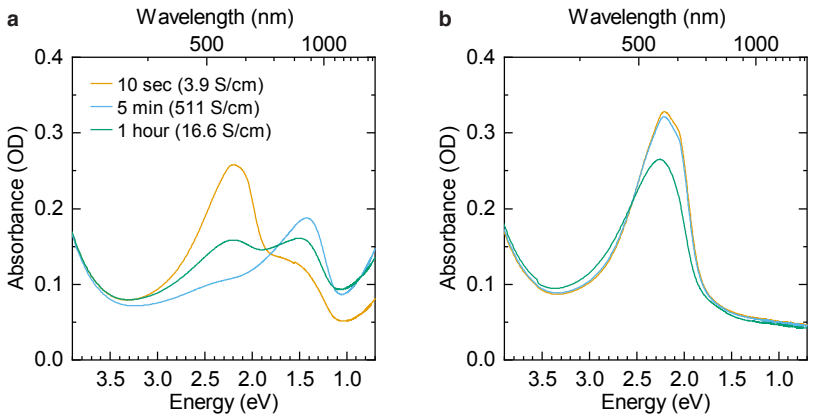

Figure S16: **Effect of excessively long doping times with a non-innocent dopant** a) UV-vis-NIR spectra of PBTTT films doped with 10/0.1 mM LiTFSI / CAN for varying times; film conductivity is indicated in the legend. b) UV-vis-NIR spectra of the films in (a) after dedoping with diethylamine (10 % v/v in acetone, 3.5 hours).

In our initial studies, we explored a much wider range of doping times, ranging up to an hour. These extended exposure times appeared to induce significant polymer degradation. Figure S16 shows UV-vis-NIR spectra of samples ion exchange doped using CAN, a fairly strong, non-innocent dopant, for varying exposure times. After dedoping, the films doped for 5 minutes showed only slightly worse recovery than those doped for 10 seconds, indicating a relatively low amount of irreversible oxidization. However, the film doped for 1 hour shows extremely poor $\pi-\pi^*$ recovery and complete loss of resolvable vibronic features in the absorption spectrum. This loss of vibronic structure is often associated with disorder, consistent with the low electrical conductivity observed in this film (16.6 S/cm for 1 hr exposure, c.f. 511 S/cm for 5 min exposure). This strong degradation was observed even in electrochemically gated films (Figure 5d, main paper), and thus is not entirely due to off-target reactivity of dopant molecules. To prevent these degradation effects from introducing ambiguity into our results, we therefore limited our doping times to a maximum of 5 minutes.

References

[1] Ian E. Jacobs, Erik W. Aasen, Julia L. Oliveira, Tayane N. Fonseca, John D. Roehling, Jun Li, Gwangwu Zhang, Matthew P. Augustine, Mark Mascal, and Adam J. Moule. Comparison of solution-mixed and sequentially processed p3ht:f4tcnq films: Effect of doping-induced aggregation on film morphology. *Journal of Materials Chemistry C*, 4(16):3454–3466, 2016.

[2] Jun Li, Correy Koshnick, Souleymane O. Diallo, Sophia Ackling, David M. Huang, Ian E. Jacobs, Thomas F. Harrelson, Kunlun Hong, Guangwu Zhang, Joseph Beckett, Mark Mascal, and Adam J. Moulé. Quantitative measurements of the temperature-dependent microscopic and macroscopic dynamics of a molecular dopant in a conjugated polymer. *Macromolecules*, 50(14):5476–5489, 07 2017.

[3] John H. Burke and Matthew J. Bird. Energetics and escape of interchain-delocalized ion pairs in nonpolar media. *Advanced Materials*, 31(12):1806863, 2020/05/21 2019.

[4] V. I. Arkhipov, E. V. Emelianova, P. Heremans, and H. Bässler. Analytic model of carrier mobility in doped disordered organic semiconductors. *Physical Review B*, 72(23):235202–, 12 2005.

[5] Friedrich G Helfferich. *Ion exchange*. Courier Corporation, 1995.

[6] Jing Li, Ivan Duchemin, Otello Maria Roscioni, Pascal Friederich, Marie Anderson, Enrico Da Como, Gabriele Kociok-Köhn, Wolfgang Wenzel, Claudio Zannoni, David Beljonne, Xavier Blase, and Gabriele D'Avino. Host dependence of the electron affinity of molecular dopants. *Materials Horizons*, 6(1):107–114, 2019.

[7] Robert R Gagne, Carl A Koval, and George C Lisensky. Ferrocene as an internal standard for electrochemical measurements. *Inorganic Chemistry*, 19(9):2854–2855, 1980.

[8] Claudia M. Cardona, Wei Li, Angel E. Kaifer, David Stockdale, and Guillermo C. Bazan. Electrochemical considerations for determining absolute frontier orbital energy levels of conjugated polymers for solar cell applications. *Advanced Materials*, 23(20):2367–2371, 2020/07/13 2011.

[9] Robin E. M. Willems, Christ H. L. Weijtens, Xander de Vries, Reinder Coehoorn, and RenéA. J. Janssen. Relating frontier orbital energies from voltammetry and photoelectron spectroscopy to the open-circuit voltage of organic solar cells. *Advanced Energy Materials*, 9(10):1803677, 2020/11/09 2019.

[10] Berthold Wegner, Lutz Grubert, Chercka Dennis, Andreas Opitz, Adriana Röttger, Yadong Zhang, Stephen Barlow, Seth R. Marder, Stefan Hecht, Klaus Müllen, and Norbert Koch. Predicting the yield of ion pair formation in molecular electrical doping: redox-potentials versus ionization energy/electron affinity. *Journal of Materials Chemistry C*, 7(44):13839–13848, 2019.

[11] Noémie Elgrishi, Kelley J. Rountree, Brian D. McCarthy, Eric S. Rountree, Thomas T. Eisenhart, and Jillian L. Dempsey. A practical beginner's guide to cyclic voltammetry. *Journal of Chemical Education*, 95(2):197–206, 02 2018.

[12] Eli M. Espinoza, John A. Clark, Joey Soliman, James B. Derr, Maryann Morales, and Valentine I. Vullev. Practical aspects of cyclic voltammetry: How to estimate reduction potentials when irreversibility prevails. *Journal of The Electrochemical Society*, 166(5):H3175–H3187, 2019.

[13] Weihua Liu, Barbara Etschmann, Joël Brugger, Leone Spiccia, Garry Foran, and Brent McInnes. Uv–vis spectrophotometric and xafs studies of ferric chloride complexes in hyper-saline licl solutions at 25–90 °c. *Chemical Geology*, 231(4):326–349, 2006.

[14] G. J. Brealey and Norbert Uri. Photochemical oxidation-reduction and photocatalysis. the photochemical activity of $fecl_4^-$ in alcohol as oxidizing agent and as catalyst. *The Journal of Chemical Physics*, 20(2):257–262, 2020/11/11 1952.

[15] Terry B. Swanson and Victor W. Laurie. Electron magnetic resonance and electronic spectra of tetrachloroferrate(iii) ion in nonaqueous solution1. *The Journal of Physical Chemistry*, 69(1):244–250, 01 1965.

[16] Byron. Kratochvil and Robert. Long. Iron(iii)-(ii) couple in acetonitrile. oxidation of thiocyanate by iron(iii). *Analytical Chemistry*, 42(1):43–46, 01 1970.

[17] Zhiming Liang, Yadong Zhang, Maryam Souri, Xuyi Luo, Alex M. Boehm, Ruipeng Li, Yan Zhang, Tairan Wang, Doo-Young Kim, Jianguo Mei, Seth R. Marder, and Kenneth R. Graham. Influence of dopant size and electron affinity on the electrical conductivity and thermoelectric properties of a series of conjugated polymers. *Journal of Materials Chemistry A*, 6(34):16495–16505, 2018.

[18] Ian E. Jacobs and Adam J. Moulé. Controlling molecular doping in organic semiconductors. *Advanced Materials*, page 1703063, 2017.

[19] Yevhen Karpov, Tim Erdmann, Ivan Raguzin, Mahmoud Al-Hussein, Marcus Binner, Uwe Lappan, Manfred Stamm, Kirill L. Gerasimov, Tetyana Beryozkina, Vasiliy Bakulev, Denis V. Anokhin, Dimitri A. Ivanov, Florian Günther, Sibylle Gemming, Gotthard Seifert, Brigitte Voit, Riccardo Di Pietro, and Anton Kiriy. High conductivity in molecularly p-doped diketopyrrolopyrrole-based polymer: The

impact of a high dopant strength and good structural order. *Advanced Materials*, 28(28):6003–6010, 2016.

[20] Andrew J Ferguson, Obadiah G Reid, Sanjini U Nanayakkara, Rachelle Ihly, and Jeffrey L Blackburn. Efficiency of charge-transfer doping in organic semiconductors probed with quantitative microwave and direct-current conductance. *The journal of physical chemistry letters*, 9(23):6864–6870, 2018.

[21] Peter Atkins and Tina Overton. *Shriver and Atkins' inorganic chemistry*. Oxford University Press, USA, 2010.

[22] RE Bozak. Photochemistry in the metallocenes. *Advances in photochemistry*, 8:227–244, 1971.

[23] David Kiefer, Renee Kroon, Anna I. Hofmann, Hengda Sun, Xianjie Liu, Alexander Giovannitti, Dominik Stegerer, Alexander Cano, Jonna Hynynen, Liyang Yu, Yadong Zhang, Dingqi Nai, Thomas F. Harrelson, Michael Sommer, Adam J. Moulé, Martijn Kemerink, Seth R. Marder, Iain McCulloch, Mats Fahlman, Simone Fabiano, and Christian Müller. Double doping of conjugated polymers with monomer molecular dopants. *Nature Materials*, 18(2):149–155, 2019.

[24] Peter A. Finn, Ian E. Jacobs, John Armitage, Ruiheng Wu, Bryan D. Paulsen, Mark Freeley, Matteo Palma, Jonathan Rivnay, Henning Sirringhaus, and Christian B. Nielsen. Effect of polar side chains on neutral and p-doped polythiophene. *Journal of Materials Chemistry C*, pages –, 2020.

[25] Phillip K. Koech, Asanga B. Padmaperuma, Liang Wang, James S. Swensen, Evgueni Polikarpov, Jens T. Darsell, James E. Rainbolt, and Daniel J. Gaspar. Synthesis and application of 1,3,4,5,7,8-hexafluorotetracyanonaphthoquinodimethane (f6-tnap): A conductivity dopant for organic light-emitting devices. *Chemistry of Materials*, 22(13):3926–3932, 07 2010.

[26] Vishnu Vijayakumar, Pablo Durand, Huiyan Zeng, Viktoriia Untilova, Laurent Herrmann, Patrick Algayer, Nicolas Leclerc, and Martin Brinkmann. Influence of dopant size and doping method on the structure and thermoelectric properties of pbttt films doped with f6tcnnq and f4tcnq. *Journal of Materials Chemistry C*, pages –, 2020.

[27] Tattiro Fujinaoa, Mutsuo Koyama, and Toshttaka Hori. The organic solvent effect on phosphomolybdic acid and its analytical application. *Talanta*, 18(9):960–962, 1971.

[28] Nobuyuki. Tanaka, Kei. Unoura, and Eiki. Itabashi. Voltammetric and spectroelectrochemical studies of dodecamolybdophosphoric acid in aqueous and water-dioxane solutions at a gold-minigrid optically transparent thin-layer electrode. *Inorganic Chemistry*, 21(4):1662–1666, 04 1982.

[29] Swagat K. Mohapatra, Yadong Zhang, Bhupinder Sandhu, Marina S. Fonari, Tatiana V. Timofeeva, Seth R. Marder, and Stephen Barlow. Synthesis, characterization, and crystal structures of molybdenum complexes of unsymmetrical electron-poor dithiolene ligands. *Polyhedron*, 116:88–95, 2016.

[30] Yabing Qi, Tissa Sajoto, Stephen Barlow, Eung-Gun Kim, Jean-Luc Brédas, Seth R. Marder, and Antoine Kahn. Use of a high electron-affinity molybdenum dithiolene complex to p-dope hole-transport layers. *Journal of the American Chemical Society*, 131(35):12530–12531, 09 2009.

[31] Kun Wang, Jonathan M. McConnachie, and Edward I. Stiefel. Syntheses of metal dithiolene complexes from thiometalates by induced internal redox reactions. *Inorganic Chemistry*, 38(19):4334–4341, 09 1999.

[32] Anita L. Arduini, Maureen Garnett, Robert C. Thompson, and Tony C. T. Wong. Magnetic and spectral studies on cobalt(ii) and copper(ii) salts of methylsulfuric, trifluoromethylsulfuric, and paratolylsulfuric acids. *Canadian Journal of Chemistry*, 53(24):3812–3819, 2020/11/12 1975.

[33] A. Paul, M. Mulholland, and M. S. Zaman. Ultraviolet absorption of cerium(iii) and cerium(iv) in some simple glasses. *Journal of Materials Science*, 11(11):2082–2086, 1976.

[34] Tadamichi Fukunaga. Negatively substituted trimethylenecyclopropane dianions. *Journal of the American Chemical Society*, 98(2):610–611, 01 1976.

[35] David Neusser, Claudia Malacrida, Michal Kern, Yannic M. Gross, Joris van Slageren, and Sabine Ludwigs. High conductivities of disordered p3ht films by an electrochemical doping strategy. *Chemistry of Materials*, 32(14):6003–6013, 07 2020.

[36] Lucas Q. Flagg, Rajiv Giridharagopal, Jiajie Guo, and David S. Ginger. Anion-dependent doping and charge transport in organic electrochemical transistors. *Chemistry of Materials*, 30(15):5380–5389, 08 2018.

[37] Yu Yamashita, Junto Tsurumi, Masahiro Ohno, Ryo Fujimoto, Shohei Kumagai, Tadanori Kurosawa, Toshihiro Okamoto, Jun Takeya, and Shun Watanabe. Efficient molecular doping of polymeric semiconductors driven by anion exchange. *Nature*, 572(7771):634–638, 2019.

[38] Elayne M. Thomas, Kelly A. Peterson, Alex H. Balzer, Dakota Rawlings, Natalie Stingelin, Rachel A. Segalman, and Michael L. Chabinyc. Effects of counter-ion size on delocalization of carriers and stability of doped semiconducting polymers. *Advanced Electronic Materials*, n/a(n/a):2000595, 2020/11/03 2020.

[39] Cedric Maton, Nils De Vos, and Christian V. Stevens. Ionic liquid thermal stabilities: decomposition mechanisms and analysis tools. *Chemical Society Reviews*, 42(13):5963–5977, 2013.

[40] Kristen E. Watts, Bharati Neelamraju, Erin L. Ratcliff, and Jeanne E. Pemberton. Stability of charge transfer states in f4tcnq-doped p3ht. *Chemistry of Materials*, 31(17):6986–6994, 09 2019.